Astron. Astrophys. 343, 585–598 (1999)

ASTRONOMY
AND
ASTROPHYSICS

Low and high velocity SiO emission around young stellar objects

C. Codella[1], **R. Bachiller**[1], **and B. Reipurth**[2]

[1] Observatorio Astronomico Nacional (IGN), Apartado 1143, E-28800 Alcalá de Henares (Madrid), Spain
[2] CASA, University of Colorado, Campus Box 389, Boulder, CO 80309, USA

Received 11 August 1998 / Accepted 11 November 1998

Abstract. We present a multiline mm-wave survey of SiO emission towards a sample of star-forming regions associated with molecular and Herbig-Haro outflows. The sample includes sources in the northern and southern hemispheres. We extensively mapped some particularly interesting objects (IRAS 00338+6312, HH7–11 and CepA). The high detection rate in the sample (52%) confirms that the SiO emission is closely associated with outflows. There exists a trend so that the more intense SiO sources are associated with higher luminosities, with an average $L_{\rm SiO}/L_{\rm IR}$ ratio of $1.8\,10^{-10}$.

The SiO lines exhibit a variety of profiles, ranging from narrow lines (1–3 km s^{-1} width) at ambient velocities to broad profiles (10–20 km s^{-1}), with complex profiles consisting of a blend of low and high velocity components as intermediate stages. In the regions where SiO was mapped, the low velocity SiO emission comes from regions definitely offset from the position where the high velocity emission is present, indicating that the *low* and *high* velocity SiO emissions trace two distinct regimes. The SiO abundances are different in those two regimes: we estimate that typical SiO abundances are $\simeq 10^{-9}$-10^{-8} in the high velocity components, but they decrease by two orders of magnitude (10^{-11}-10^{-10}) when SiO is detected at low velocities.

The hydrogen volume densities estimated from the multiline SiO observations are in the range 10^5 to fews 10^6 cm^{-3}, in both the low and the high velocity regimes, indicating that all the SiO emission arises in shock-compressed regions. We argue that the different observed SiO profiles could be caused by an evolutionary effect: the SiO molecules produced at high velocities could be slowed down because of their interaction with the surrounding gas before they stick onto the dust grains. However, the possibility that the low velocity SiO emission is due to slow shocks cannot be ruled out, but this would require the presence of a small amount of silicon compounds on the dust grain mantles.

Key words: ISM: clouds – ISM: jets and outflows – ISM: molecules – radio lines: ISM

Send offprint requests to: C. Codella

1. Introduction

Silicon monoxide (SiO) emission is usually not seen toward quiescent regions in molecular clouds. Ziurys et al. (1989) placed an upper limit of the SiO fractional abundance near 10^{-12} in such regions in nearby molecular complexes. However, SiO can be enhanced by several orders of magnitude at the heads and along the axes of some molecular outflows from low-mass young stellar objects (YSOs) (e.g. Martín-Pintado et al. 1992, Bachiller 1996 and references therein). In these cases, SiO can be found at velocities and positions different from those of the ambient gas emission (e.g. Bachiller et al. 1991, McMullin et al. 1994b). Moreover, measurements done towards outflows near high-mass star-foming regions (SFRs) also show the association of SiO with shocked regions (Downes et al. 1982, Wright et al. 1983, Acord et al. 1997). Taking all together, these observations have led to the belief that shock processing of dust can release silicon-bearing molecules to the gas. Such silicon species will eventually result in a significant increase of the SiO abundance in the gas phase. Recent theoretical studies confirm this picture (Schilke et al. 1997, Caselli et al. 1997, Pineau des Forêts et al. 1997).

Since the number of SFRs detected as SiO sources is quite limited so far, and some prototypical outflow sources remained to be observed, we decided to carry out a survey of the SiO thermal emission J = 2–1, J = 3–2 and J = 5–4 lines towards a sample of SFRs located in both hemispheres.

The observed sample contains sources of different luminosities (from about 1 $L_\odot$ to $\sim$ $2\,10^4$ $L_\odot$) associated with molecular outflows and well-known Herbig-Haro (HH) objects (L1448/IRS 2, L1455/IRS 1, HH12, HH7–11, HH366, HH300, L1551/IRS 5, HH26, HH47C, HH56/57, Serp/FIRS 1, HH100, CepA) and H_2O masers (IRAS 00338+6312, IRAS 20050+2720, IRAS 21334+5039). In addition, IRAS 21004+7811, which is classified as a Class I YSO (Claussen et al. 1996), has been also observed. It is worth noting that CepA, HH7–11 and Serpens have been already investigated through a few SiO spectra by Martín-Pintado et al. (1992), Koo (1990) and McMullin et al. (1994a), respectively. However, for some of these sources, high quality SiO data and maps are reported here for the first time. The aims of this project are: (i) to verify the association of SiO with shocked gas of

molecular outflows, (ii) to check the possible dependence of SiO enhancement on the luminosity of the newly born stars and (iii) to try to find a relationship of spectral and/or positional SiO features with the evolutionary stage of a SFR.

2. Observations

The northern hemisphere observations were carried out with the IRAM 30-m telescope at Pico Veleta (near Granada, Spain) during several periods in 1990, 1992, 1997 and 1998. At the rest frequency of the J = 2–1, J = 3–2 and J = 5–4 v=0 lines (86846.998 MHz, 130268.702 MHz and 217104.935 MHz) the HPBW is 26″, 17″ and 13″, the beam efficiency is 0.6, 0.6 and 0.45, and typical system temperatures were around 500 K, 600 K and 800 K, respectively. The observations were made by position switching. Pointing was checked every hour by observing nearby planets or continuum sources and it was found to be accurate to within 3″. As spectrometers, the 1 MHz filter bank, split into three parts of 2 × 256 and 512 channels, was used to allow simultaneous observations of the SiO lines. It provided a velocity resolution of 3.45, 2.30 and 1.38 km s^{-1} for the J = 2–1, J = 3–2 and J = 5–4 lines, respectively. During the 1990 and 1992 runs, the J = 3–2 and J = 5–4 lines were observed, while during 1997 and 1998 also the J = 2–1 line was included. For some sources of the present sample, the J = 3–2 line was observed with the 256×100 kHz channel filterbank, with a resolution of 0.23 km s^{-1}. During the 1997 and 1998 runs, the three SiO lines were simultaneously observed also using an autocorrelator, providing a resolution of 0.13, 0.18 and 0.11 km s^{-1} at 86, 130 and 217 GHz. When necessary, the spectra obtained using the autocorrelator were smoothed to a velocity resolution of 0.53, 0.72 and 0.86 km s^{-1}. The spectra were calibrated with the standard chopper wheel method and are reported here in units of mean-beam brightness temperature ($T_{\rm MB}$).

The southern hemisphere observations were carried out with the 15-m Swedish-ESO Submillimeter Telescope (SEST) at La Silla (Chile) during May 1996. The J=2–1 and J=3–2 v=0 SiO lines were observed. The HPBW is respectively 57″ and 40″, the beam efficiency is 0.75 and 0.68, while typical system temperatures ranged between 150 K and 200 K. The observations were made in beam switching mode and the pointing was found to be accurate to within 3″ (rms). An Acousto Optical Spectrometer (AOS) with 2000 channels was used, giving a velocity resolution of 0.15 and 0.10 km s^{-1} at 86 and 130 GHz, respectively.

Table 1 summarizes the regions where SiO emission was searched for.

Table 1. Regions investigated through SiO observations

Name	α (1950)	δ (1950)	Telescope[a]
IRAS 00338+6312	00 33 53.3	+63 12 32	PV
L1448/IRS 2	03 22 17.9	+30 34 40	PV
L1455/IRS 1	03 24 34.9	+30 02 36	PV
HH12	03 25 52.1	+31 09 51	PV
HH7–11(SVS 13)	03 25 58.3	+31 05 47	PV
HH366W1	03 43 49.7	+32 36 04	PV
HH366E1	03 45 22.2	+32 46 25	PV
HH300A	04 22 21.7	+24 16 32	PV
HH300C	04 22 37.2	+24 19 59	PV
HH300D	04 23 56.4	+24 37 13	PV
L1551/IRS 5	04 28 40.1	+18 01 40	PV
HH26	05 43 31.2	–00 15 42	PV
HH47C	08 24 05.6	–50 51 47	SE
HH56/57	16 28 56.8	–44 49 17	SE
Serp/FIRS 1	18 27 17.5	+01 13 15	SE
HH100	18 58 28.7	–37 02 33	SE
IRAS 20050+2720	20 05 02.5	+27 20 09	PV
IRAS 21004+7811	21 00 28.4	+78 11 13	PV
IRAS 21334+5039	21 33 24.0	+50 39 43	PV
CepA	22 54 19.0	+61 45 47	PV

[a] Observed with the 30-m Pico Veleta antenna (PV) or with the 15-m SEST antenna (SE).

3. Results

The results of our search are summarized in Fig. 1 and in the Tables 2 and 3. Table 2 lists the observed SiO parameters for the detected sources: the mean-brightness temperature, the noise of the spectrum (r.m.s.), the LSR velocity ($v_{\rm LSR}$), the FWHM linewidth and the integrated SiO flux ($F_{\rm SiO}$). The fit parameters have been obtained assuming for each spectrum a single gaussian profile. Table 3 reports the detection limits (3 r.m.s.) for the objects not detected as SiO emitters. Of the 17 SFRs, 9 (52%) have been detected in at least one SiO line. This confirms that SiO emission is associated with SFRs and, in particular, with molecular outflows. However, if we limit the detection rate to the search towards the positions of the HH knots, it reduces to about 25%. On the other hand, the detection rate reaches $\simeq$ 75% if we take into account just the observations towards the CO lobes of the outflows excluding the HH knots. The low detection rate for our HH subsample could simply be due to the decrease of the column density of the molecular gas which, on the other hand, permits the detection of the HH knots in the optical. However, we have also to take into account the possibility that the lack of SiO emission towards the HH objects reflect different physical conditions with respect to those of the molecular gas traced by silicon monoxide: i.e. the temperatures associated with the HH shocks are probably too high to maintain the molecules associated.

For several sources of the present sample a search for SiO emission towards positions offset from the coordinates listed in Table 1 has been performed. In addition, we present extended maps for IRAS 00338+6312, HH7–11 and CepA.

3.1. Comments on individual objects

3.1.1. IRAS 00338+6312

IRAS 00338+6312 in L1287 is a source of IR luminosity $\sim$ 1100 $L_{\odot}$ associated with a bipolar CO outflow (Yang et al. 1991) and with a water maser (Fiebig 1995). A map of the SiO J = 3–2

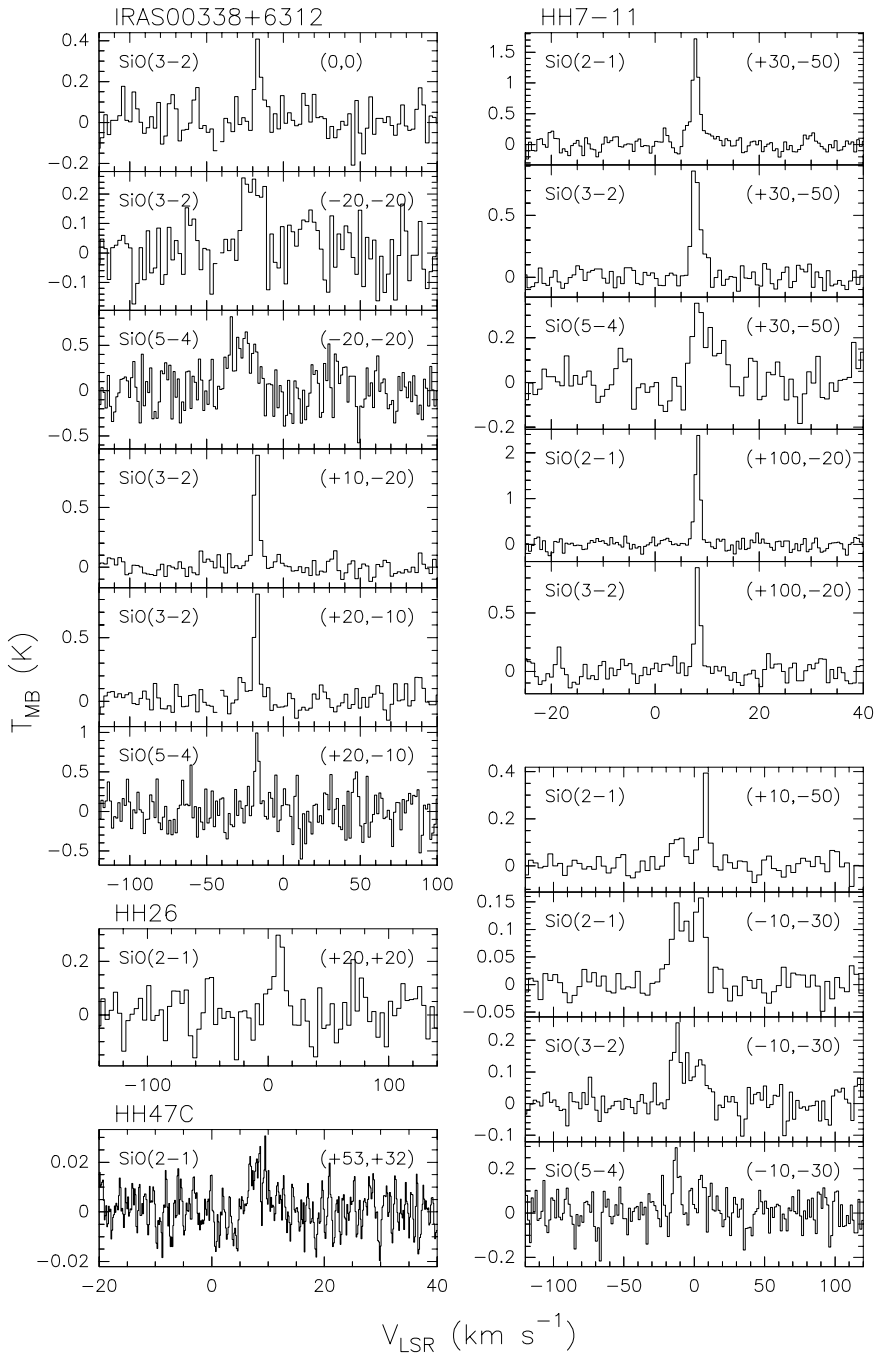

Fig. 1. Silicon monoxide spectra whose parameters are reported in Table 1. Source name, SiO line, and angular offset position (in arcseconds) are indicated.

line (Fig. 2) shows a quite extended irregular structure. A more detailed picture of the SiO structure can be obtained from Fig. 3 which clearly indicates that the high velocity emission comes from a region that is offset from the location of the bulk of the emission at central LSR velocities. Comparing the present maps with that in CO (J = 1–0) given by Yang et al. (1991; see their Fig. 3), we can see that the high velocity SiO emission is detected towards positions associated with CO wing emission. Comparison of the SiO J = 3–2 spectra shown in Fig. 1 demonstrate that the FWHM linewidth at the (+10″,–20″) position is about 3 km s^{-1}, while it is larger ($\simeq$ 13 km s^{-1}) at the (–20″,–20″) position. Moreover, the J = 5–4 line has been detected only towards the (+20″,–10″) and (–20″,–20″) positions with linewidths of about 3 and 13 km s^{-1}, respectively. In summary, we find two kind of line profiles around IRAS 00338+6312: broad lines associated with the CO outflow, and narrow lines distributed in a more irregular manner over the molecular cloud.

3.1.2. HH7–11

The HH7–11 system, a chain of bright HH knots about 1′ long near NGC 1333, is one of the best studied HH complexes (for references see, e.g., Reipurth 1994). The HH7–11 objects are associated with the blueshifted lobe of a high-velocity CO outflow

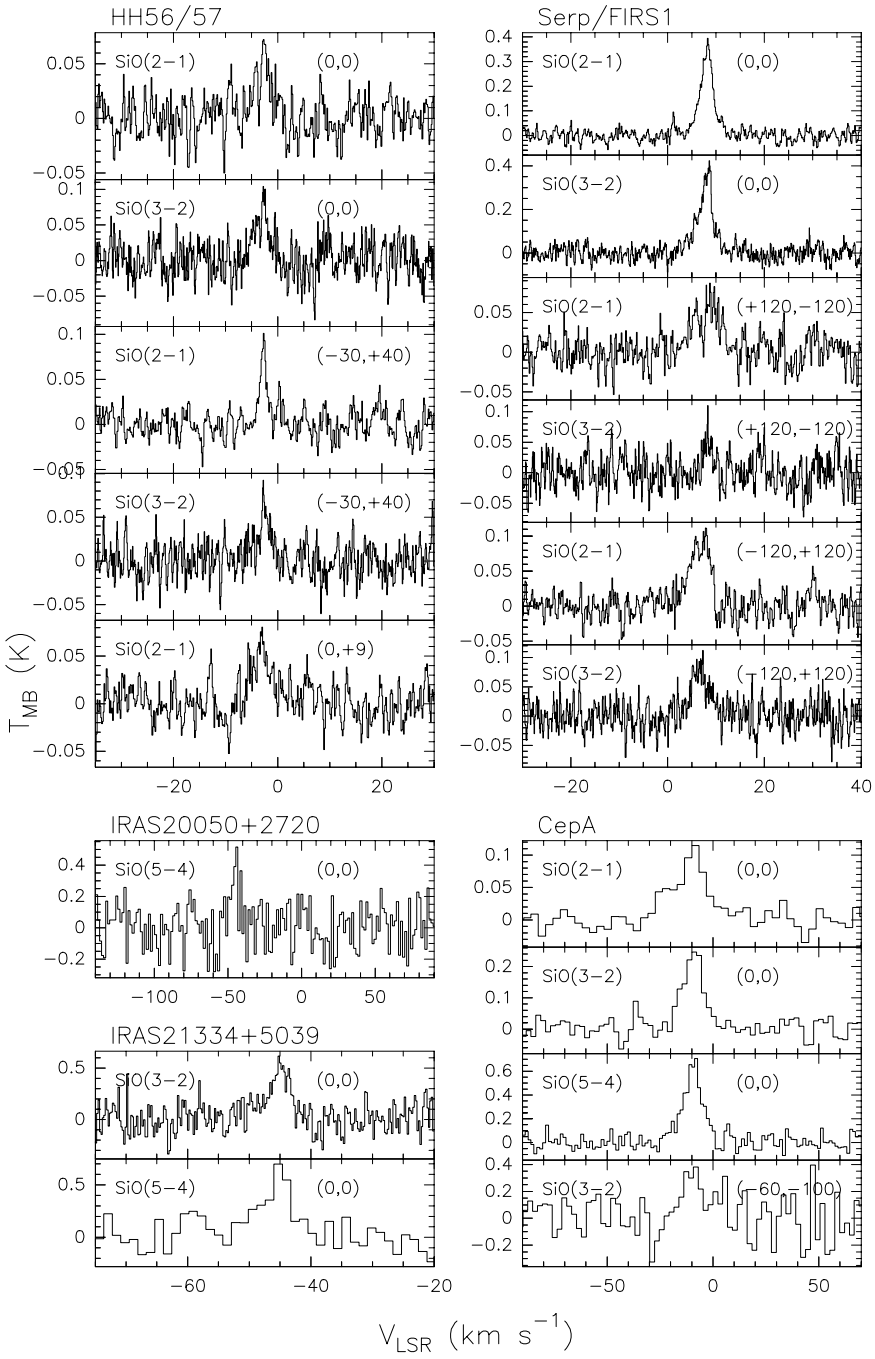

Fig. 1. (continued)

(Snell & Edwards 1981, Bachiller & Cernicharo 1990, Masson et al. 1990, Koo 1990), which is also bright in H_2 (Stapelfeldt et al. 1991, Hodapp & Ladd 1995). The HH7–11 area contains three water masers at 22.2 GHz, as well as at 183.3 GHz (Cernicharo et al. 1996 and references therein). For a long time the source of the outflow has been presumed to be the partly obscured star SVS 13 ($L \simeq 115\ L_{\odot}$; Molinari et al. 1993). However, Rodríguez et al. (1997) have recently revealed through centimetric VLA observations another radio source previously undetected at other wavelengths, which lies only 6″ SW from SVS 13 and is a likely driving candidate.

Maps of the HH7–11 region have been obtained in the three SiO lines using measurements spaced every 20″; the main SiO clump has been sampled every 10″. The analysis done using the autocorrelator (see Sect. 2.1) reveals the presence of a *narrow line* component (linewidth ~ 1 km s^{-1} for the J = 2–1 transition) centered at about $v_{\rm LSR} = +8$ km s^{-1}, whose spatial distribution is shown in Fig. 4. This emission delineates a kind of fragmented filament of size $\sim 150''$ (~ 0.25 pc). The main maximum is located at (+30″, –50″) relative to SVS 13, while other maxima can be detected along the main structure: one is roughly located at the end of the HH chain. There is no clear overlap of this SiO structure either with the HH flow (filled triangles) driven

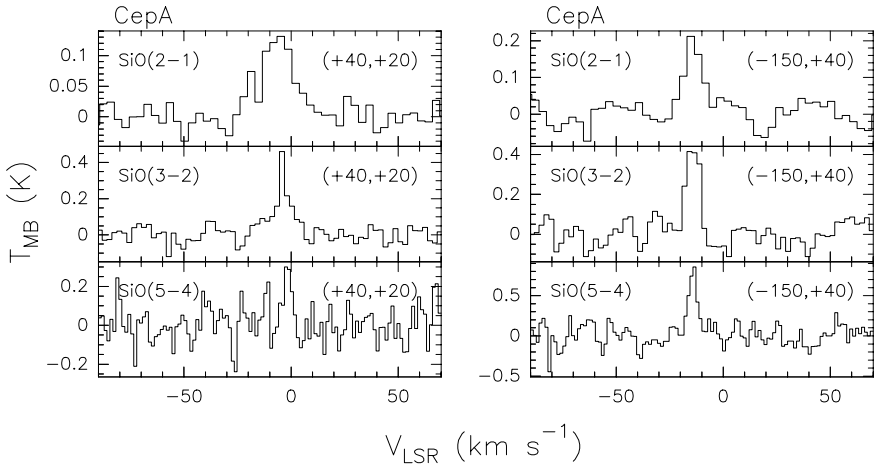

Fig. 1. (continued)

Table 2. Observed parameters for the detected SiO sources

Name	Offset[a] (″)	Line	$T_{\rm MB}$ (K)	rms (K)	$v_{\rm LSR}$ (km s^{-1})	FWHM (km s^{-1})	$F_{\rm SiO}$ (K km s^{-1})
IRAS 00338+6312	0,0	3–2	0.51 (0.20)	0.21	–17.50 (0.23)	2.60 (0.47)	2.43 (1.74)
	0,0	5–4	–	0.23	–	–	–
	–20,–20	3–2	0.26 (0.08)	0.08	–20.34 (1.25)	13.38 (2.45)	3.58 (0.66)
	–20,–20	5–4	0.54 (0.18)	0.22	–26.80 (1.44)	18.32 (2.81)	10.30 (2.00)
	+10,–20	3–2	1.17 (0.11)	0.13	–17.49 (0.07)	3.08 (0.17)	4.99 (1.08)
	+10,–20	5–4	–	0.13	–	–	–
	+20,–10	3–2	1.15 (0.20)	0.22	–17.49 (0.10)	2.75 (0.22)	4.48 (1.82)
	+20,–10	5–4	1.01 (0.01)	0.21	–17.16 (0.30)	3.05 (0.70)	4.30 (1.35)
HH7–11	–10,–10	2–1	–	0.10	–	–	–
	–10,–10	3–2	–	0.06	–	–	–
	–10,–10	5–4	–	0.08	–	–	–
	+30,–50	2–1	1.22 (0.08)	0.09	+7.76 (0.04)	1.63 (0.10)	3.27 (0.30)
	+30,–50	3–2	0.92 (0.07)	0.07	+7.79 (0.06)	1.88 (0.21)	1.83 (0.20)
	+30,–50	5–4	0.22 (0.09)	0.07	+9.31 (0.44)	4.97 (0.90)	1.40 (0.23)
	+100,–20	2–1	2.37 (0.09)	0.10	+8.17 (0.02)	1.17 (0.06)	3.28 (0.32)
	+100,–20	3–2	0.90 (0.05)	0.08	+8.18 (0.06)	1.17 (0.11)	1.12 (0.21)
	+100,–20	5–4	–	0.08	–	–	–
	+10,–50	2–1	0.12 (0.01)	0.03	–11.83 (1.12)	11.61 (2.96)	{ 3.71 (0.37)
	+10,–50	2–1	0.39 (0.08)	0.03	+8.11 (0.27)	5.12 (0.45)	
	–10,–30	2–1	0.13 (0.02)	0.02	–10.23 (1.00)	15.21 (2.51)	{ 3.82 (0.37)
	–10,–30	2–1	0.16 (0.02)	0.02	+4.51 (0.55)	7.82 (1.14)	
	–10,–30	3–2	0.19 (0.03)	0.03	–12.29 (0.50)	8.18 (1.56)	{ 3.59 (0.28)
	–10,–30	3–2	0.13 (0.03)	0.03	+4.25 (0.27)	13.10 (2.31)	
	–10,–30	5–4	0.27 (0.04)	0.06	–12.84 (0.41)	3.87 (0.21)	2.47 (0.41)
HH26	0,0	2–1	–	0.07	–	–	–
	0,0	3–2	–	0.10	–	–	–
	0,0	5–4	–	0.51	–	–	–
	+20,+20	2–1	0.29 (0.03)	0.07	–9.02 (1.15)	10.45 (3.07)	2.18 (0.88)
	+20,+20	3–2	–	0.09	–	–	–
	+20,+20	5–4	–	0.49	–	–	–
HH47C	0,0	2–1	–	0.01	–	–	–
	0,0	3–2	–	0.01	–	–	–
	+53,+32	2–1	0.02 (0.01)	0.01	+8.45 (0.29)	4.00 (0.64)	0.07 (0.03)
	+53,+32	3–2	–	0.01	–	–	–
HH56/57	0,0[b]	2–1	0.05 (0.02)	0.02	–2.67 (0.18)	3.74 (0.42)	0.19 (0.02)
	0,0[b]	3–2	0.07 (0.02)	0.02	–3.03 (0.14)	4.07 (0.32)	0.28 (0.06)
	0,+9[c]	2–1	0.07 (0.02)	0.01	–3.12 (0.19)	4.97 (0.50)	0.29 (0.03)
	–30,+40[d]	2–1	0.09 (0.01)	0.02	–2.75 (0.05)	1.61 (0.15)	0.19 (0.03)
	–30,+40[d]	3–2	0.06 (0.02)	0.02	–2.41 (0.11)	1.97 (0.31)	0.11 (0.03)

Table 2. (continued)

Name	Offset[a] ($''$)	Line	$T_{\rm MB}$ (K)	rms (K)	$v_{\rm LSR}$ (km s^{-1})	FWHM (km s^{-1})	$F_{\rm SiO}$ (K km s^{-1})
Serp/FIRS 1	0,0	2–1	0.33 (0.03)	0.02	+8.12 (0.03)	2.98 (0.06)	1.23 (0.05)
	0,0	3–2	0.33 (0.04)	0.03	+7.96 (0.04)	3.32 (0.08)	1.28 (0.06)
	+120,–120	2–1	0.04 (0.02)	0.02	+8.47 (0.28)	5.44 (0.53)	0.28 (0.03)
	+120,–120	3–2	0.06 (0.02)	0.03	+8.35 (0.14)	1.84 (0.33)	0.09 (0.06)
	–120,+120	2–1	0.09 (0.02)	0.01	+6.62 (0.11)	4.67 (0.24)	0.36 (0.03)
	–120,+120	3–2	0.08 (0.02)	0.02	+6.63 (0.14)	4.27 (0.36)	0.32 (0.06)
IRAS 20050+2720	0,0	3–2	–	0.17	–	–	–
	0,0	5–4	0.38 (0.14)	0.14	–45.10 (0.78)	7.19 (2.27)	2.68 (1.27)
IRAS 21334+5039	0,0	3–2	0.49 (0.09)	0.14	–45.03 (0.20)	4.05 (0.57)	2.36 (0.37)
	0,0	5–4	0.56 (0.10)	0.13	–45.54 (0.48)	6.17 (1.33)	4.70 (0.84)
CepA	0,0	2–1	0.13 (0.02)	0.02	–6.09 (0.73)	17.75 (1.77)	2.30 (0.21)
	0,0	3–2	0.35 (0.07)	0.04	–3.78 (0.35)	7.88 (1.48)	2.89 (0.26)
	0,0	5–4	0.31 (0.04)	0.08	–1.64 (0.47)	4.15 (1.05)	0.62 (0.43)
	+40,+20	2–1	0.10 (0.01)	0.01	–10.62 (0.84)	19.93 (2.21)	1.95 (0.21)
	+40,+20	3–2	0.24 (0.01)	0.03	–9.39 (0.44)	11.50 (1.05)	2.71 (0.26)
	+40,+20	5–4	0.63 (0.06)	0.07	–9.42 (0.32)	10.72 (0.81)	6.04 (0.43)
	–60,–100	3–2	0.32 (0.07)	0.14	–9.15 (2.80)	13.34 (5.20)	3.87 (0.94)
	–150,+40	2–1	0.20 (0.08)	0.04	–14.09 (0.59)	9.40 (1.42)	2.28 (0.21)
	–150,+40	3–2	0.46 (0.04)	0.07	–14.26 (0.34)	6.85(0.65)	2.71 (0.26)
	–150,+40	5–4	0.83 (0.05)	0.15	–14.18 (0.28)	4.74 (0.68)	4.41 (0.43)

[a] Position offset with respect to the positions listed in Table 1; [b] HH57; [c] V346 Nor; [d] HH56.

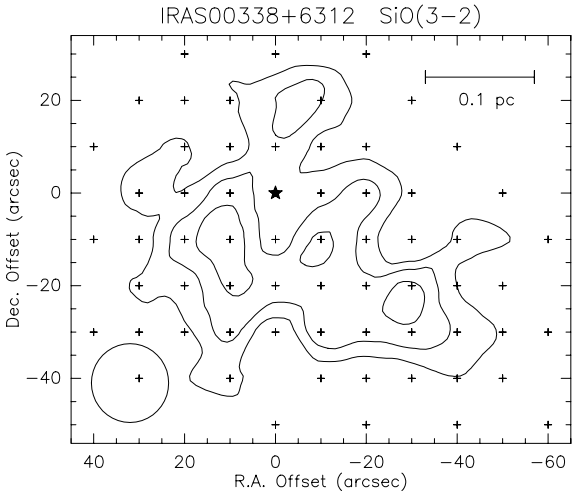

Fig. 2. Contour map of the integrated J = 3–2 SiO emission towards IRAS 00338+6312. The small crosses mark the observed positions, the empty circle shows the IRAM beam (HPBW) and the filled star identifies the IRAS source. The contour levels range from 2.13 (3 σ) to 4.97 K km s^{-1} by step of 2 σ, where σ is the r.m.s. of the map.

Table 3. Detection limits ($T_{\rm MB}$ (K) scale, 3 r.m.s.) for the not detected sources

Name	Offset[a]	2–1	3–2	5–4
L1448/IRS 2	0,0	–	0.36	8.84
L1455/IRS 1	0,0	–	0.63	0.72
HH12	0,0	0.12	0.09	0.12
HH366W1	0,0	0.09	0.18	0.18
HH366E1	0,0	0.09	0.09	0.15
HH300A	0,0	0.12	0.12	0.45
HH300C	0,0	0.12	0.15	0.54
HH300D	0,0	0.15	0.15	0.66
L1551/IRS 5	0,0	–	0.33	1.08
	+113,+1[b]	0.21	0.30	1.29
	–232,–18[c]	0.15	0.21	0.78
	–420,–420	–	0.45	1.17
	–240,–240	–	0.51	1.74
	–120,–120	–	0.87	2.79
	+120,+120	–	0.99	2.61
	+240,+240	–	0.48	1.65
	+440,+440	–	0.45	1.20
HH100	0,0	0.06	0.03	–
IRAS 21004+7811	0,0	–	0.78	0.87

[a] Position offset with respect to the positions listed in Table 1
[b] L1551-2E
[c] L1551-4W

from the YSO or with the extremely high velocity CO outflow reported, e.g., by Bachiller & Cernicharo (1990; see their Fig. 9). In fact, SiO lies in a structure that seems complementary to that of the high velocity CO outflow/HH jet.

Moreover, the information coming from the analysis of the spectra observed with the 1MHz filter bank (larger bandwidth and lower resolution than the autocorrelator spectra) shows that there is also a *broad line* component (FWHM $\simeq$ 12–15 km s^{-1} for the J = 2–1 transition). This broad line is well seen, for instance, in the spectra at (+10$''$,–50$''$) and (-10$''$,–30$''$) (see

Fig. 1). Fig. 5 shows the spatial distribution of the broad SiO emission: it is clear that it comes from a region definitely offset with respect to that emitting narrow SiO lines. Therefore, the present results indicate the occurrence of two distinct SiO regimes with different spatial and spectral distributions. Recent interferometric observations demonstrate that the broad velocity component is due to a newly identified bipolar outflow (Bachiller et al. 1998).

Our observations are in agreement with the single SiO spectrum reported by Koo (1990). In addition, Lefloch et al. (1998) have very recently reported a complete map of the NGC 1333 complex in the SiO lines which is in good agreement with our data. They also pointed out the presence of the SiO low and high velocity components in this particular source, and discussed their possible origin (see Sect. 6).

Fig. 6 shows the position-velocity map obtained through the SiO J = 2–1 data (i.e. those observed with the best spectral resolution: 0.53 km s^{-1}, using the autocorrelator data) along a direction roughly perpendicular to that of the HH flow and of the high-velocity CO outflow. A systematic variation from +8.83 km s^{-1} (+110″,+10″) to +7.18 km s^{-1} (+10″, –90″) seems to be present, suggesting that SiO emission is coming from a kind of irregular molecular shell stirred by the outflow, the SW part moving towards the observer with a projected velocity larger than that of the NE part. Moreover, the analysis of the linewidths of the narrow J = 2–1 SiO lines reveals that whereas the values for the majority of the positions investigated are around 1 km s^{-1}, those regarding the main clump centered at about (+30″,–50″) are between 1.6 and 2.6 km s^{-1}. This effect, confirmed also by the J = 3–2 linewidths, suggests different physical conditions for the main clump with respect to the rest of the SiO structure and indicates a possible connection with the high velocity CO outflow whose boundaries, according to Bachiller & Cernicharo (1990), are located close to the clump itself.

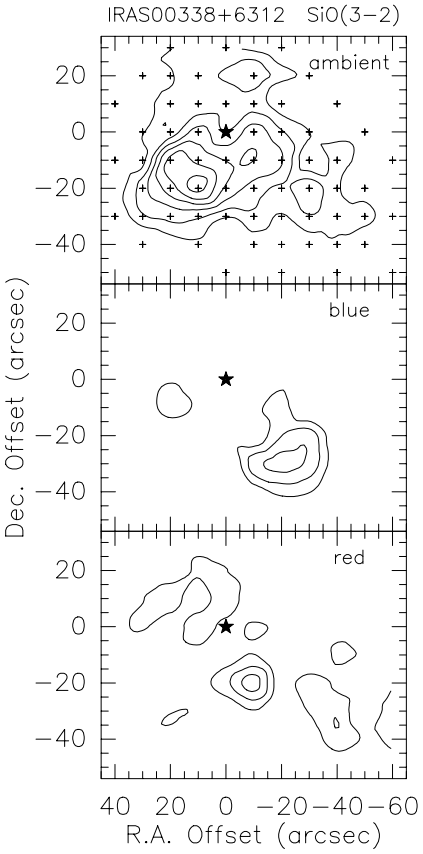

Fig. 3. Contour map of the integrated J = 3–2 SiO emission towards IRAS 00338+6312 integrated from –21 km s^{-1} to –15 km s^{-1} (*upper panel*), from –31 km s^{-1} to –21 km s^{-1} (*center panel*) and from –15 km s^{-1} to –5 km s^{-1} (*lower panel*). Symbols are as in Fig. 2. The contour levels range from 0.84 to 3.64 K km s^{-1} (*upper panel*) and from 0.96 to 2.24 K km s^{-1} (*center* and *lower panels*). The first contours and the steps correspond to 3 and 2 σ, respectively.

3.1.3. CepA

Cepheus A is a well known SFR, within a much larger molecular cloud, associated with ultracompact (UC) H II regions, infrared sources, H_2O maser emission, HH objects and with a multipolar molecular outflow (e.g. Garay et al. 1996 and references therein). The luminosity based on the IRAS counterpart (22543+6145) is 1.2 10^4 $L_\odot$ (Felli et al. 1992). Narayanan & Walker (1996) reported high sensitivity maps of the CO outflow. They found extended high velocity (HV) CO lobes of age $\simeq 10^5$ yr oriented along the east-west axis and a smaller pair of younger (< 5000 yr) extremely high velocity (EHV) CO lobes (see their Fig. 2). The association of CepA with SiO emission has already been reported by Martín-Pintado et al. (1992), who observed a region of $\sim$40″ in SiO. We obtained maps of the CepA regions connected with the two bipolar outflows in the three SiO lines using a 20″ spacing. Fig. 7 shows a sort of SiO filament with two clumps near the HW2 object (marked by a filled star), thought to be the driving source of the CepA outflow system (see Narayanan & Walker 1996 and references therein). Moreover, another clump is present at the (–150″, +40″) position, at the end of the lobes of the more extended CO outflow. The comparison between the SiO emission of the different clumps shows that the SiO emission at (–150″, +40″) is characterized by a smaller linewidth ($\simeq$ 9 km s^{-1} for the J = 2–1 emission) and a different LSR velocity ($\simeq$ –14 km s^{-1}) with respect to that of the central position (about 20 km s^{-1} and –10 km s^{-1}, respectively), suggesting different physical gas conditions. In particular, the CepA spectra reported in Fig. 1 shows the occurrence of high velocity wings, covering the same range of velocity of the HV CO outflow: we have blue and red emission at the (+40″, +20″) position and blue emission at (0, 0).

Finally, we have searched for SiO (J = 3–2) emission towards 40 positions around the (0, –2′) position which to our knowledge is not directly associated with any radio/infrared source. These positions lie along the direction roughly perpendicular to the CO outflows. We report a tentative detection towards a single position in the region offset from the molecular outflows (see Fig. 1); the gaussian fit of the line gives a FWHM linewidth of about 13 km s^{-1} and a LSR velocity of about –9 km s^{-1}.

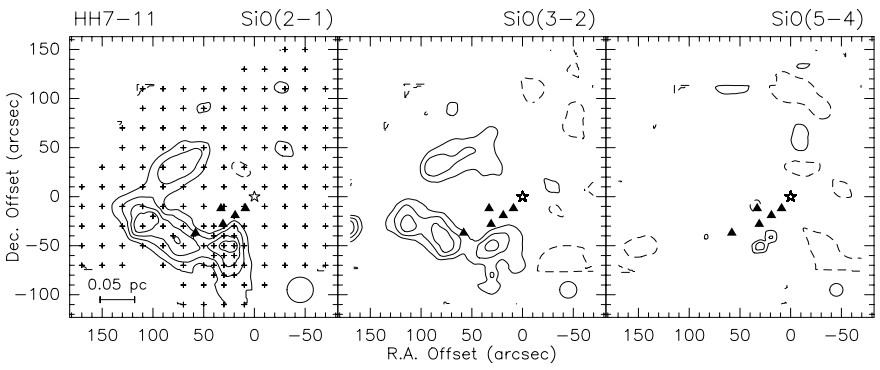

Fig. 4. Contour map of the J = 2–1, J = 3–2 and J = 5–4 SiO narrow line (integrated) emission at $\simeq +8$ km s^{-1} towards the HH7–11 region. The small crosses mark the observed positions, the empty circles show the IRAM beams (HPBW), the filled triangles are for the HH positions, while the star is for the SVS 13 source. The contour levels range from –0.96 to 2.88 K km s^{-1} (left panel), from –0.63 to 1.89 K km s^{-1} (center panel) and from –0.69 to 1.15 K km s^{-1} (right panel). The first contours and the steps correspond to 3 σ (–3 σ, dashed line) and 2 σ, respectively.

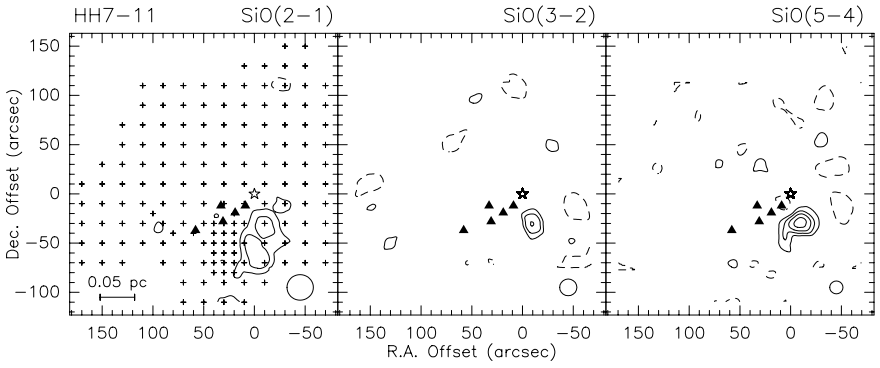

Fig. 5. Contour map of the J = 2–1, J = 3–2 and J = 5–4 SiO broad line (integrated) emission at $\simeq -12$ km s^{-1} towards the HH7–11 region. Symbols are drawn as in Fig. 4. The contour levels range from –1.05 to 1.75 K km s^{-1} (*left panel*), from –1.05 to 2.45 K km s^{-1} (*center panel*) and from –0.78 to 2.34 K km s^{-1} (*right panel*). The first contours and the steps correspond to 3 σ (–3 σ, dashed line) and 2 σ, respectively.

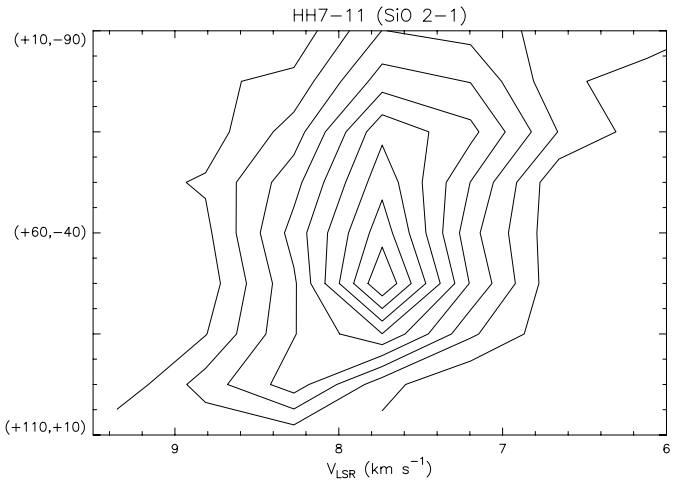

Fig. 6. Position-velocity map of SiO J = 2–1 in HH7–11 obtained from a cut along the NE-SW direction, i.e. perpendicular to that of the HH flow and of the high-velocity CO outflows reported by Bachiller & Cernicharo (1990. The offset positions used to trace the axis are reported. First contour and contour interval are 0.23 K.

3.1.4. Other sources

The bipolar outflow in the Taurus cloud L1551 is associated with several HH objects and with an infrared source (IRS 5) of about 30 $L_{\odot}$ (Beichman & Harris 1981). We have searched for SiO emission without success along a strip throughout the main axis of the L1551 bipolar outflow, from (–420″, –420″) to (+440″, +440″) offset from IRS 5, towards 52 positions. Moreover, we have investigated two clumps (L1551-2E, L1551-4W) along the edges of the bipolar outflow where bright and high-velocity CS emission has been observed by Plambeck & Snell (1995). No SiO emission has been detected (Table 2).

HH26 is located in the southern part of the complex NGC 2068, in the Orion molecular cloud L1630. It is closely connected with the the HH25 object and with a bipolar CO outflow (Gibb & Heaton 1993). Near HH26 lies the IRAS source 05435-0015 ($L \simeq 20\ L_{\odot}$; Felli et al. 1992). However, Davis et al. (1997) have recently detected a near-IR (NIR) source (HH26IR) which lies at the geometric centre of the HH26 CO outflow and is suspected to be the driving source of the outflow motion. The authors have also presented H_2 S(1) line-emission knots located along the CO emission. For HH26 we have performed a 5-points map using measurements spaced by 20″. SiO J = 2–1 emission has only been detected towards the (+20″,+20″) position, in the direction of the blue lobe.

The HH46/47 object is one of the major bipolar highly collimated Herbig-Haro jets with several bow shocks emerging from an infrared source with $L \simeq 24\ L_{\odot}$ (Molinari et al. 1993) in a Bok globule in the Gum nebula (e.g. Reipurth & Heathcote 1991). In particular, two arc-shaped HH-objects, HH47D and HH47C, are assumed to be the bow shocks of the jets. We have searched for SiO towards HH47C and towards the main axis of the red lobe of the CO outflow detected by Chernin & Masson (1991) and Olberg et al. (1992). SiO J = 2–1 emission has been detected towards the molecular outflow, while no SiO emission has been observed coming directly from the HH bow shock at the end of the jet.

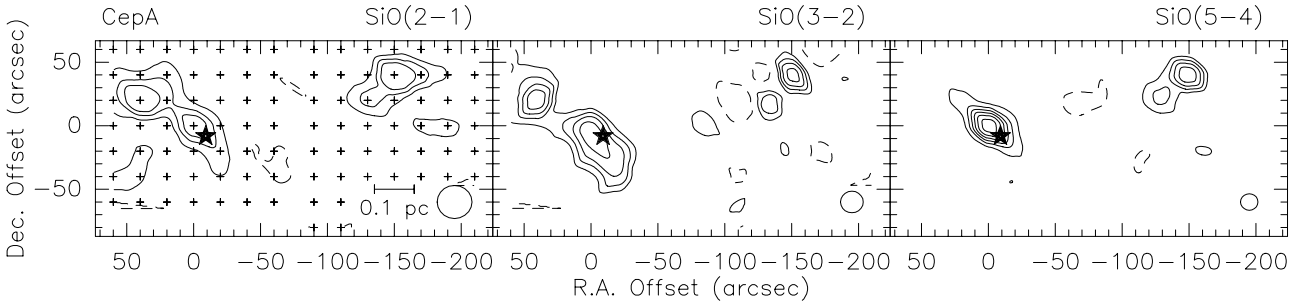

Fig. 7. Contour map of the J = 2–1, J = 3–2 and J = 5–4 SiO (integrated) emission towards the CepA region. The small crosses mark the observed positions, the empty circles show the IRAM beams (HPBW), while the filled star is for the HW2 source. The contour levels range from –0.66 to 1.98 K km s^{-1} (*left panel*), from –0.84 to 3.08 K km s^{-1} (*center panel*) and from –1.29 to 5.59 K km s^{-1} (*right panel*). The first contours and the steps correspond to 3 σ (–3 σ, dashed line) and 2 σ, respectively.

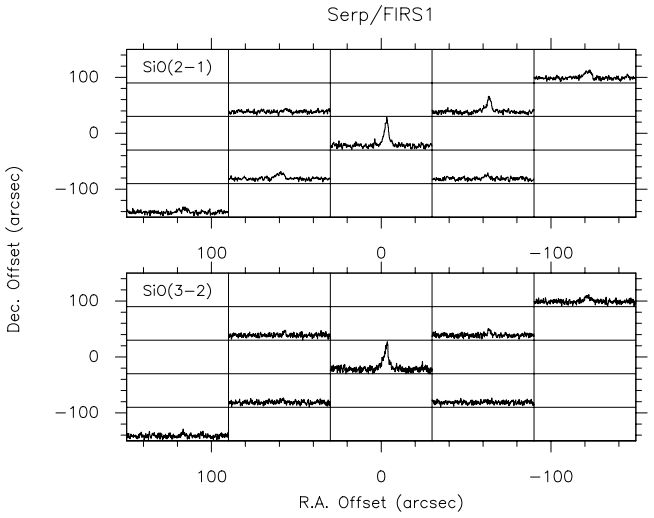

Fig. 8. SiO J = 2–1 (*upper panel*) and J = 3–2 (*lower panel*) spectra of Serp/FIRS 1: the LSR velocity range from –25 to +35 km s^{-1}, while the intensity from –0.06 to +0.30 K ($T_{\rm MB}$ scale; see Fig. 1).

HH56 is a bright bow shock located in a bipolar collimated outflow; nearby, a quite small knot (HH57) is present (e.g. Reipurth et al. 1997) The suspected energy source of HH57 is a quite bright infrared source (L = 288 $L_{\odot}$) whose optical counterpart has been identified as an FU Orionis star, V346 Nor (Graham & Frogel 1985). SiO emission was detected towards both HH objects as well as towards V346 Nor.

The Serpens molecular cloud is a nearby low and intermediate mass SFR extensively investigated through multiwavelengths observations (e.g. Eiroa 1991). The FIR/SMM1 object (L = 79 $L_{\odot}$) is associated with an IRAS source (18273+0113), a 22 GHz water maser source (Palla & Giovanardi 1989), a radio continuum source, a jet-like H_2 nebulosity and a CO outflow (e.g. Torrelles et al. 1992, Curiel et al. 1993, 1996). For FIR/SMM1 we have performed a 7-points SiO map using measurements spaced by 1′. The corresponding J = 2–1 and J = 3–2 spectra are shown in Fig. 8, which shows that the strongest emission comes from the central position (FIR/SMM1), where the outflow is also seen in ammonia emission (Curiel et al. 1996), and that it decreases along the direction of the radio jet (NW-SE). Positions corresponding to directions perpendicular to the radio jet are definitely weaker SiO emitters. It is worth noting that the observed SiO gas is associated with different velocities at different map positions (e.g. see Table 2), indicating that with the present spectra we are investigating different portions of the molecular gas present in the region. Finally, we note that the J = 2–1 feature observed towards the central position presents a possible weak line ($T_{\rm MB}$ = 0.61 K; S/N = 3) at $v_{\rm LSR}$ = +1.2 km s^{-1}, suggesting the occurrence of a SiO clump moving with a velocity of about 7 km s^{-1} with respect to the bulk of the SiO emission from FIRS 1.

IRAS 20050+2720 is a source of 260 $L_{\odot}$ placed in the Cygnus Rift and associated with a 22 GHz maser source (Palla et al. 1991) and with a high velocity multipolar CO outflow (Bachiller et al. 1995). SiO emission has been searched for towards several positions of the northern part of the CO outflow in a region of about 180″×80″ and it has been detected at the IRAS coordinates. A possible SiO J = 5–4 feature towards the IRAS source is at about -45 km s^{-1}, a velocity quite different from that of the ambient cloud ($\simeq$ +6 km s^{-1}; e.g. Wilking et al. 1989), and with FWHM $\simeq$ 7 km s^{-1}, supporting the association of SiO with shocked regions.

IRAS 21334+5039 is a source of 2.1 10^4 $L_{\odot}$ associated with an UCH II region (McCutcheon et al. 1991), and with a 22 GHz maser source (Churchwell et al. 1990). A search towards a region of 40″×50″ has been performed: SiO emission has been detected only towards the position of the IRAS source.

4. Derived gas parameters and SiO abundances

For the sources detected in two or three SiO lines, it is possible to estimate total SiO column densities ($N_{\rm SiO}$) as well as estimates of the kinetic temperatures ($T_{\rm k}$) and of hydrogen densities ($n_{\rm H_2}$) by means of statistical-equilibrium calculations. We have used a Large Velocity Gradient (LVG) code which considers the SiO-H_2 collision rates given by Turner et al. (1992) and levels up to J = 20 (Walmsley, private communication). For the sources for which a map of the SiO emission is available, the physical parameters can be estimated at different map positions. In sources where *low and high* velocity components were detected, we performed a separate analysis for each component.

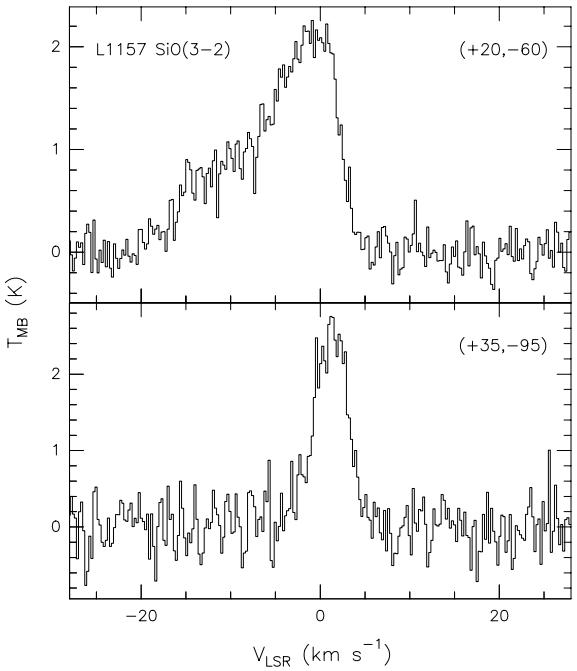

Fig. 9. Silicon monoxide spectra (J = 3–2) of two positions in the blueshifted lobe of the L1157 molecular outflow (Bachiller & Pérez Gutiérrez 1997). The angular offset position (from the driving source, L1557mm, in arcseconds) are indicated. The lower panel shows the position thought to be older, since it is more distant from the central star.

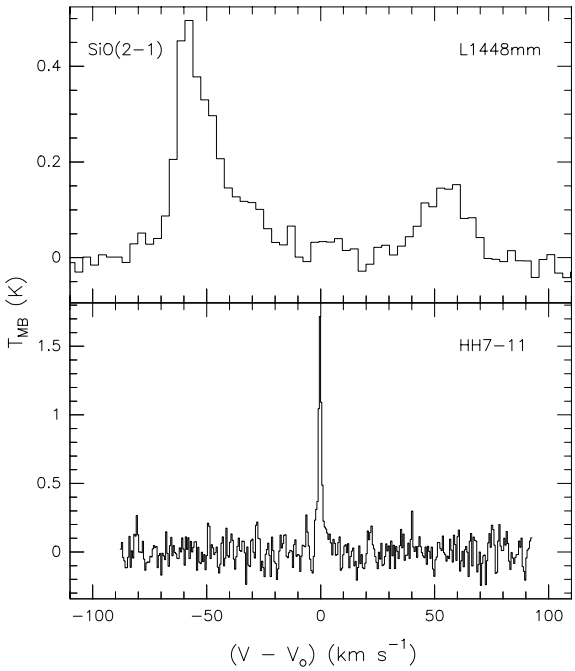

Fig. 10. Silicon monoxide spectra (J = 2–1) of L1448mm (*upper panel*, Bachiller et al. 1991) and HH7–11 (*lower panel*). The horizontal axis is the velocity measured with respect to the ambient gas ($v_{\rm o}$).

The statistical-equilibrium calculations have been performed using the values of the intensities of the SiO spectra at different wavelengths expressed in the mean-beam brightness temperature scale, without correction due to the beam filling factor. The excitation conditions will remain the same if the source size is comparable to the beam sizes, or slightly smaller, and we have similar filling factors for the different SiO transitions. However, if the source sizes were definitely smaller than the three beamwidths, i.e. sort of point-like sources, the LVG code would lead to an overestimate of the excitation conditions. In the other extreme, we could assume that the sources are definitely larger than the beamwidths. In such a case, it would be better to work on the spectra expressed in $T_{\rm A}^{\star}$, i.e. the antenna temperature corrected for atmospheric losses, which is representative of the radiation detected by the whole antenna pattern and not just by the mean beam. As a first approximation, we assume sources with a SiO emission homogeneously distributed throughout their projected extension. In this case, using the $T_{\rm MB}$ values (instead of $T_{\rm A}^{\star}$) leads to an overestimate (although less than in the first case) of the excitation conditions. In order to test the uncertainties given by working with the mean-beam brightness temperature, statistical-equilibrium calculations have been run in these two extreme cases. We found, as expected, lower excitation conditions in both cases: the kinetic temperatures and the hydrogen densities can be reduced by factors of 1.2 and 2.0, respectively, at such extreme situations. Moreover, the total SiO column densities can decrease up to a factor of 9. However, if we consider just the latter case (extended sources) the densities can only be reduced by a factor of up to 1.3 (2 for the column densities). We believe that the sources discussed here represent an intermediate case between the two extreme situations discussed, allowing us to consider the use of $T_{\rm MB}$ a reasonable approximation.

In the case of IRAS 00338+6312, both low and high velocity components are well seen (see Sect. 3.1.1). The high velocity component has $T_{\rm k} \simeq 120$ K and $n_{\rm H_2} \geq 10^6$ cm^{-3}. On the other hand, if we assume that the low velocity SiO component is associated with the ambient quiescent gas (as suggested by the similar central velocities) traced for instance through the ammonia emission (e.g. Estalella et al. 1993), we find temperatures of about 20 K and densities of about fews 10^6 cm^{-3}. This assumption is also supported by the fact that the SiO J=3–2 and NH_3(1,1) lines have narrow linewidths (2.75 and 1.93 km s^{-1}, respectively). The total SiO column densities are in the range between 4 10^{12} and 1 10^{13} cm^{-2}.

For HH7–11 it is also possible to distinguish between the low and high velocity components. For the low velocity main maximum located at (+30″, –50″) from SVS 13, we found low temperatures ($T_{\rm k} \simeq 20$ K) and densities $\leq 10^5$ cm^{-3}. On the other hand, toward the (–10″, –30″) position, where also the high velocity component is present, we found different physical conditions for both components: the low velocity component has similar physical parameters to those derived toward (+30″, –50″), whereas the high velocity component has slightly higher temperatures (50 K) and higher densities, $n_{\rm H_2} \simeq 6\,10^6$ cm^{-3}.

For CepA, temperatures about 150 K, densities about fews 10^6 cm^{-3} and SiO column densities about 10^{13} cm^{-2} have been

found for the SiO emission around the (0, 0) positions, whereas lower temperatures ($\simeq 80$ K) have been found for the SiO clump located at (–150″, +40″).

The values obtained for HH56/57, Serp/FIRS 1 and IRAS 21334+5039 indicate densities around 10^5 and $5\,10^6\,\mathrm{cm}^{-3}$ and SiO column densities between a few times 10^{11} (HH56/57) and $\simeq 10^{12}\,\mathrm{cm}^{-2}$ (Serp/FIRS 1, IRAS 21334+5039). For the sources detected as SiO sources in just one line, we have estimated the total column densities assuming optically thin emission (supported by the low values of optical depths found using the statistical-equilibrium calculations) and values for the excitation temperature based on those calculated where multiline SiO data are available. The $N_{\rm SiO}$ values obtained are $\simeq 10^{11}$ (HH47C), $\leq 10^{12}$ (IRAS 20050+2720) and $\simeq 10^{13}\,\mathrm{cm}^{-2}$ (HH26). The assumption of the excitation values produces uncertainties less than a factor of two in the column density estimates.

With the aim of obtaining an estimate of the SiO abundances, the H_2 column densities towards the positions where the $N_{\rm SiO}$ values are available have been derived by comparing with the CO, ^{13}CO and C^{18}O data reported in the literature. For the *low velocity* component, observations regarding the last two isotopes of the carbon monoxide have been used, assuming [^{13}CO/H_2] = $1.1\,10^{-6}$ and [C^{18}O/H_2] = $2.0\,10^{-7}$. The derived SiO abundances lie between $3\,10^{-11}$ and $2\,10^{-10}$. For the *high velocity* components, the H_2 column densities have been derived from CO data and with the assumption [CO/H_2] = $1.0\,10^{-4}$. The derived values yield SiO abundances in the range between $3\,10^{-9}$ and $3\,10^{-8}$. Thus, we find an increase of the abundances of SiO at velocities associated with outflows with respect to the values calculated for the SiO components with velocities similar to the ambient medium. In particular, for IRAS 00338+6312, we find the SiO abundance equal to $2\,10^{-10}$ for the narrow component at the ambient velocity and to $3\,10^{-9}$ for the broader component. In the case of HH7–11, values of $8\,10^{-11}$ (low velocity emission) and $3\,10^{-8}$ (high velocity emission) have been derived. These latter results are in good agreement with recent estimates from Lefloch et al. (1998) at different positions of the NGC 1333 molecular cloud.

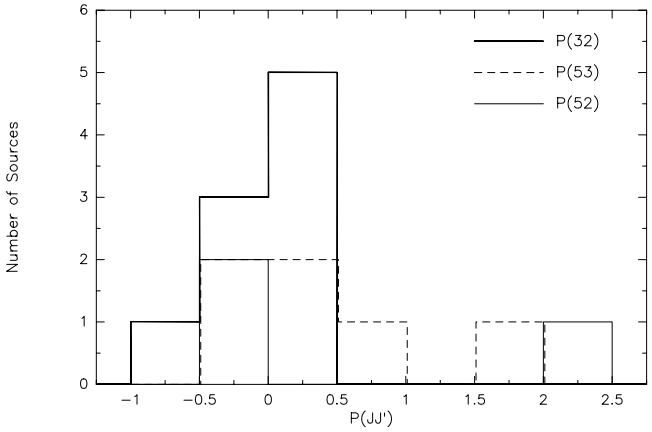

Fig. 11. The distribution of the parameter $P(JJ^{'})$ (see text) regarding the three SiO transition J = 2–1, 3–2 and 5–4: the thick continuous line is for P(32), the dashed one stands for P(53), while the thin continuous one is for P(52).

5. Discussion

5.1. Origin of the low and high velocity SiO components

Comparison of the SiO spectra reported here with those produced by other molecular species in the same sources suggests that a variety of SiO profile shapes exists: from narrow lines at velocities close to the ambient one to broad profiles at much higher velocities. It is worth noting that different SiO profiles have been detected towards different objects as well as towards different positions of the map of some sources, like IRAS 00338+6312, HH7–11 and CepA.

Although the high velocity SiO components are closely linked with molecular outflows, the origin of the low velocity line emission is less clear. Our LVG analysis shows that all the SiO emission is associated with high density material ($\sim 10^5$-$10^6\,\mathrm{cm}^{-3}$), in agreement with the results reported by Martín-Pintado et al. (1992) for a sample of molecular outflows. This seems to confirm that all SiO emission (at high and low velocities) arises in regions compressed by shocks. However, in the case of the *low* velocity component this appears to be somewhat contradictory, since one would in principle expect the shocked gas to exhibit *high* velocities. In the case of NGC 1333, this problem has recently been considered by Lefloch et al. (1998), who proposed that the low velocity SiO component could trace the interaction of the protostellar outflows with stationary dense clumps in the ambient cloud. In the following we explore alternative explanations to this puzzling phenomenon.

We discuss here the origin of the low velocity SiO emission in the context of the evolution of bipolar outflows. We first consider whether the low velocity SiO emission could be due to molecules which, once produced by shocks at high velocities, slow down till the value of the ambient velocity as they interact with the surrounding gas, loosing momentum. In fact, some additional observations seem to confirm the validity of this mechanism. Fig. 9 shows SiO spectra obtained toward two positions in the blueshifted lobe of the L1157 molecular outflow (Bachiller & Pérez Gutiérrez 1997). The lower panel shows the position thought to be older, since it is more distant from the driving star L1157 (see the angular offset, in arcseconds). It appears that the broader emission is connected with the younger position, whereas the narrower spectrum traces the older gas probably slowed down at the end of the lobe by the interaction with the surrounding molecular cloud. A similar behaviour in the SiO profiles is observed along the L1448 outflow (Bachiller et al. 1991). Another even more extreme case of low velocity SiO emission at the end of a bipolar CO flow is that of IRAS 03282+3035 (Bachiller et al. 1994).

In this scenario, a recent ejection in a molecular outflow should manifest itself by SiO emission just at high LSR velocities, without a low velocity component, similar to what is observed very close to L1448-mm (Fig. 10 upper panel, from Bachiller et al. 1991): there is no emission at the ambient velocity, while two high velocity components are observed to

arise from the bipolar outflow. For comparison, we also show in Fig. 10 the SiO emission from the vicinity of HH7–11 (see Sect. 3.1.2), where only a very narrow ambient component is present, without any emission at higher velocities. It is tempting to suggest that HH7–11 is an evolved version of this recent ejection in the L1448 outflow, and that the differences in the profiles reflect the case in which the molecules produced by shock-chemistry have reached the ambient velocity, probably the latest evolutionary stage of the outflow traced by SiO before its complete depletion onto dust grains. This picture is in agreement with that discussed by Chernin & Masson (1993) who justify the SO emission at low velocity towards NGC 2071 as the residual of molecules produced in faster shocks but already slowed down by sweeping up ambient material.

A possible check of this scenario comes from the comparison of two time-scales: $t_{\rm des}$, the time needed for the destruction of the gas-phase SiO, and $t_{\rm dis}$, the time required for SiO produced at high velocity to slow down till velocities close to the ambient one.

SiO could be removed from the gas-phase by direct accretion onto grains in about 10^4 yr (e.g. Bergin et al. 1998). However, Pineau des Forêts et al. (1997) have recently suggested that SiO could be more efficiently destroyed by reacting with OH, which is expected to be very abundant in the post-shocked gas: SiO + OH $\rightarrow$ SiO_2 + H. Eventually, SiO_2 could be eliminated from the gas-phase by accretion onto dust grains. The importance of this oxidation process is difficult to be pondered because SiO_2 is not directly observable since it has no permanent dipole moment. Nevertheless, Pineau des Forêts et al. (1997) estimate the time required to convert SiO in SiO_2 in about 10^4 yr. Thus, whatever process led to the gas-phase SiO destruction (direct accretion or oxidation), it appears that $t_{\rm des} \sim 10^4$ yr.

The time needed to slow down the SiO molecules can be estimated by assuming that the SiO clumps were spherical and homogeneous blobs with size r, mass M, mass density ρ moving at velocity v with respect to an ambient medium of mass density ρ_1. Thus, the gas drag force acting on the SiO blob can be expressed as $F_{\rm D} = \frac{1}{2} C_{\rm D} \pi r^2 \rho_1 v^2$, where $C_{\rm D}$ is a drag coefficient we put equal to unity (similarly to the assumption of Hayashi et al. 1985, in the context of dynamics of planetesimals). The dissipation time is given by

$$t_{\rm dis} = \frac{Mv}{F_{\rm D}} = \frac{2M}{\pi r^2 \rho_1 v} = \frac{8}{3} \frac{\rho}{\rho_1} \frac{r}{v}. \quad (1)$$

By assuming r = 0.05 pc (e.g. see the SiO maps of HH7–11), a ratio ρ/ρ_1 = 10 and a velocity v = 100 km s^{-1}, it results that $t_{\rm dis} \sim 1.3\,10^4$ yr.

Even considering the large uncertainties involved in the assumptions made above, the fact that $t_{\rm des} \sim t_{\rm dis} \sim 10^4$ yr indicates that the high velocity SiO molecules are slowed down at the same time as they are destroyed in the gas phase. In other words, a simultaneous decrease in both velocity and abundance is expected. The fact that the SiO abundances for the high-velocity components are observed to be two orders of magnitude higher than those found in the low-velocity component seems to confirm the scenario described above.

An alternative hypothesis for the origin of the low velocity SiO component that deserves consideration is that some significant amount of SiO were formed by slow shocks. In fact, it is generally assumed that the silicon material comes from dust grain cores and that it is necessary to fully destroy the dust grains to obtain some SiO in gas phase. However, it can not be excluded that some silicon material were mixed with the ices on the dust grain surfaces, and that slow shocks were able to inject a significant amount of silicon into the gas phase from the mantles, without completely destroying the grains.

5.2. SiO excitation as a function of the linewidth

It has been proposed that bow shocks may play a dominant role in the outflow propagation (Bachiller 1996, and references therein). However, as discussed by Lada & Fich (1996), general models of bow shocks do not provide good bipolarity, since they should create a wide cavity in the ambient cloud, and should behave similarly to an isotropic wind, creating less forward momentum than is observed. There is, however, a new family of collimated bow shock models which have the large momentum required to reproduce the basic observed feature of the outflows (Wilkin 1996, Zhang & Zheng 1997). In these models, it appears that the bow shock velocity is directed forward rather than perpendicular to its line of propagation and that the highest velocities are expected at the bow tip. As a consequence, this configuration produces a peculiar pattern in the excitation, with the highest excited material flowing at the shock head with the highest velocities. In other words, an important way to test the reliability of collimated bow shock models is to check if the gas excitation increases as the observed velocities increase. The present SiO observations can in principle be used to verify the occurrence of this effect. In order to perform this analysis we have used the parameter

$$P(JJ') = \frac{[(\Delta v)_{J-(J-1)} - (\Delta v)_{J'-(J'-1)}]}{[(\Delta v)_{J'-(J'-1)}]} \quad (2)$$

which gives an estimate, in percentage, of the difference between the linewidths, Δv, of the three observed SiO lines. The three possible combinations with J $>$ J$'$ have been calculated and shown in Fig. 11. The results listed in Table 2 have been used, except those of the position in HH7–11 where two line profiles are blended. Fig. 11 shows that, excluding the measurements of Serp/FIRS 1 and CepA, the $P(JJ')$ are positive, suggesting that lines at higher excitation are broader. The maximum of the distribution regards $P(JJ') \simeq$ 0.1–0.4, while some linewidths broadened up to very large factors are also present. We should stress that the values reported here have been calculated without taking into account the Δv fit errors. However, the trend shown in Fig. 11 seems to indicate an increasing dependence of the excitation on velocity. Of course, the limited sample used to verify this dependence does not allow us to solve the question. Moreover, we should also point out that we have neglected that the different SiO transitions have been sampled using different beamwidths and, thus, it is possible that they are

tracing different gas portions. Nevertheless, our results seem to support models in which the maximum interaction between the jet and the ambient medium (maximum excitation) happens at the highest velocities. The collimated bow shock models with very forward directed velocity fields seem to be very promising models accomplishing this requirement.

5.3. SiO and IR luminosities

As already pointed out, the luminosities of the YSOs of the present sample cover a wide range, from 1 $L_{\odot}$ to 2 10^4 $L_{\odot}$, offering a good opportunity to check if a relationship exists with SiO emission. The present results shows that there is a trend such that the more intense SiO emission regions are associated with higher luminosity sources, with an average $L_{\rm SiO}/L_{\rm IR}$ ratio of $1.8\,10^{-10}$. It is reasonable to assume that the SiO abundance enhancement is directly connected with the mechanical power of the outflow motion, $L_{\rm m}$, which, in turn, can be considered as a fraction of the total luminosity of the star(s). Felli et al. (1992), for instance, have found, for a large sample of CO molecular outflows, that the average ratio $L_{\rm m}/L_{\rm IR}$ is 10^{-3}. In a sample of well known outflows, and after correcting for the outflow inclination, Cabrit & Bertout (1992) found that this ratio can range from 10^{-3} to 0.1, and the highest ratios (up to ~ 0.3) are found toward Class 0 sources (Bachiller 1996). Thus, $L_{\rm SiO}/L_{\rm m}$ is in the range from $\simeq 10^{-9}$ to 10^{-7} and so we can roughly estimate that a fraction of about 10^{-8} of the outflow kinetic energy is dissipated through SiO emission.

6. Conclusions

A sample of SFRs associated with molecular outflows and HH objects, located in both hemispheres, has been investigated through a multiline SiO survey at mm-wavelengths. The main results are the following:

1. Of the whole sample, 52% (9 objects) have been detected as SiO sources, confirming that silicon monoxide emission is associated with SFRs and, in particular, with molecular outflows. This is a further check of the already proposed idea of SiO formation as a consequence of shock-chemistry. In particular, we do not find a strong relation between SiO emission and HH objects, although both are shock phenomena. This could be due to the low density of the molecular gas connected with HH objects or simply reflect different physical conditions, e.g. higher temperatures, with respect to those of the gas traced by SiO. Moreover, the present results shows that there is a trend of the more intense SiO sources to be associated with higher luminosities, with an average $L_{\rm SiO}/L_{\rm IR}$ ratio of $1.8\,10^{-10}$;
2. The SiO lines exhibit a variety of profile shapes: from narrow emission confined at velocities close to the ambient one to purely broad profiles, through complex profiles formed by the blend of low and high velocity lines. Different profiles can be detected towards different objects as well as towards different map positions of a SFR. Two distinct SiO emission regimes have been identified: the *high* and the *low* velocity SiO components.
3. For IRAS 00338+6312, HH7–11 and CepA, we have obtained maps of the low and high velocity SiO emission lines. In IRAS 00338+6312, the high velocity emission comes from the region where a CO outflow occurs, which is definitely offset from the position where the bulk of the low velocity emission at ambient LSR velocity is present. The maps of the HH7–11 reveal that the low velocity SiO structure is complementary to that of the molecular outflow/HH flow, perhaps suggesting that SiO in this SFR traces gas compressed by old shocks driven from the SVS 13 vicinity. The high velocity SiO emission in HH7–11 is related to a recently identified jet-like molecular outflow (Bachiller et al. 1998).
4. By means of statistical-equilibrium calculations, using a LVG code, physical parameters of the molecular gas investigated through SiO emission have been obtained. The total SiO column densities lie between 10^{11} and 10^{13} cm^{-2}, while the hydrogen densities are quite high, $\simeq 10^6$ cm^{-3}, confirming that SiO arises in regions compressed by the occurrence of shocks. The *low* and *high* SiO velocity component present different abundances: the SiO abundances are about 10^{-11}-10^{-10} at low velocities, and two orders of magnitude higher at high velocities (10^{-9}-10^{-8}).
5. The low velocity SiO emission could be due to SiO molecules which, once produced at high velocities, are slowed down because of their interaction with the surrounding quiescent gas. Another possibility is that the low velocity SiO is created by slow shocks, but this would require the presence of a significant amount of silicon on the dust grain mantles.
6. There is an indication that SiO lines at higher excitation are broader. This result is consistent with recent collimated bow shock models, in which the shock velocity is directed forward rather than perpendicular to the line of propagation and, as a consequence, the highest excited material flows at the shock head with the highest velocities.

Acknowledgements. This research has made use of the Simbad database, operated at CDS, Strasbourg, France. We are grateful to P. Caselli, M. Tafalla and M. Walmsley for helpful discussions and suggestions. We wish to thank M. Walmsley also for supplying his LVG code used for statistical-equilibrium calculations and M. Pérez Gutiérrez for his help during the observations. This research has been partially supported by Spanish DGES Grant PB96–104.

References

Acord J.M., Walmsley C.M., Churchwell E., 1997, ApJ 475, 693
Bachiller R., 1996, ARA&A 34, 111
Bachiller R., Cernicharo J., 1990, A&A 239, 276
Bachiller R., Martín-Pintado J., Fuente A., 1991, A&A 243, L21
Bachiller R., Terebey S., Jarrett T., et al., 1994, ApJ 437, 296
Bachiller R., Fuente A., Tafalla M., 1995, A&A 445, L51
Bachiller R., Pérez Gutiérrez M., 1997, ApJ 487, L93
Bachiller R., Guilloteau S., Gueth F., et al., 1998, A&A 339, L49
Beichman C., Harris S., 1981, ApJ 245, 589

Bergin E.A., Neufeld, D.A., Melnick G.J., 1998, ApJ 499, 777
Cabrit S., Bertout C., 1992, A&A 261, 274
Caselli P., Hartquist T.W., Havnes O., 1997, A&A 322, 296
Cernicharo J., Bachiller R., González-Alfonso E., 1996, A&A 305, L5
Chernin L.M., Masson C.R., 1991, ApJ 382, L93
Chernin L.M., Masson C.R., 1993, ApJ 403, L21
Churchwell E., Walmsley C.M., Cesaroni R., 1990, A&AS 83, 119
Claussen M.J., Wilking B.A., Benson P.J., et al., 1996, ApJS 106, 111
Curiel S., Rodríguez L.F., Moran M., Cantó J., 1993, ApJ 415, 191
Curiel S., Rodríguez L.F., Gómez J.F., et al., 1996, ApJ 456, 677
Davis C.J., Ray T.P., Eislöffel J., Corcoran D., 1997, A&A 324, 263
Downes D., Genzel R., Hjalmarson A., Nyman L.A., Ronnang B., 1982, ApJ 307, L65
Eiroa C., 1991, in Low Mass Star Formation in Southern Molecular Clouds, ESO Report No.11, Ed. B. Reipurth, p. 197
Estalella R., Mauersberger R., Torrelles J., et al., 1993, ApJ 419, 698
Felli M., Palagi F., Tofani G., 1992, A&A 256, 293
Fiebig D., 1995, A&A 298, 207
Garay G., Ramírez S., Rodríguez L.F., Curiel S., Torrelles J.M., 1996, ApJ 459, 193
Gibb A.G., Heaton B.D., 1993, A&A 276, 511
Graham J.A., Frogel J.A., 1985, ApJ 289, 331
Hayashi C., Nakazawa K., Nakagawa Y., 1985, in Protostars & Planets II, Eds. D.C. Black, M.S. Matthews, p. 1100, Tucson: Univ. Ariz. Press
Hodapp K.-W., Ladd E.F., 1995, ApJ 453, 715
Koo B.-C., 1990, ApJ 361, 145
Lada C.J., Fich M., 1996, ApJ 459, 638
Lefloch B., Castets A., Cernicharo J., Loinard L., 1998, ApJ 504, L109
Masson C.R., Mundy L.G., Keene J., 1990, ApJ 357, L25
McCutcheon W.H., Dewdney P.E., Purton C.R., Sato T., 1991, AJ 101, 1435
McMullin J.P., Mundy L.G., Wilking B.A., Hezel T., Blake G.A., 1994a, ApJ 424, 222
McMullin J.P., Mundy L.G., Blake G.A., 1994b, ApJ 437, 305
Martín-Pintado J., Bachiller R., Fuente A., 1992, A&A 254, 315
Molinari S., Liseau R., Lorenzetti D., 1993, A&AS 101, 59
Narayanan G., Walker C.K., 1996, ApJ 466, 844
Olberg, M., Reipurth, B., Booth, R.S., 1992, A&A 259, 252
Palla F., Giovanardi C., 1989, A&A 223, 267
Palla F., Brand J., Cesaroni R., Comoretto G., Felli M., 1991, A&A 246, 249
Pineau des Forêts G., Flower D.R., Chièze J.-P., 1997, in Herbig-Haro Flows and the Birth of Low Mass Stars, Proc. IAU Symp. 182, Eds B. Reipurth and C. Bertout, p. 199, Kluwer, Dordrecht
Plambeck R.L., Snell R.L., 1995, ApJ 446, 234
Reipurth B., 1994, A general catalogue of Herbig-Haro objects, electronically published via anon. ftp to ftp.hq.eso.org, directory /pub/Catalogs/Herbig-Haro
Reipurth, B., Heathcote, S., 1991, A&A 246, 511
Reipurth, B., Olberg, M., Gredel, R., Booth, R.S., 1997, A&A 327, 1164
Rodríguez L.F., Anglada G., Curiel S., 1997, ApJ 480, L125
Schilke P., Walmsley C.M., Pineau des Forêts G., Flower D.R., 1997, A&A 321, 293
Snell R.L., R.L., Edwards S., 1981, ApJ 303, 683
Stapelfeldt K.R., Beichman C.A., Jeff Hester J., Scoville N.Z., Gautier III T.N., 1991, ApJ 371, 226
Torrelles J.M., Gómez J.F., Curiel S., et al., 1992, ApJ 384 L59
Turner B.E., Chan K.-W., Green S., Lubowich D.A., 1992, ApJ 399, 114
Wilkin F.P., 1996, ApJ 459, L31
Wilking B.A., Mundy L.G., Blackwell J.H., Howe J.E., 1989, ApJ 345, 257
Wright M.C.H., Plambeck R.L., Vogel S.N., Ho P.T.P., Welch W.J., 1983, ApJ 267, L41
Yang J., Umemoto T., Iwata T., Fuku Y., 1991, ApJ 373, 137
Zhang Q., Zheng X., 1997, ApJ 474, 719
Ziurys L.M., Friberg P., Irvine W.M., 1989, A&A 343, 201